Smart Structures and Systems, *Vol. 24, No. 6 (2019) 803-812*
DOI: https://doi.org/10.12989/sss.2019.24.6.803

Visualization and classification of hidden defects in triplex composites used in LNG carriers by active thermography

Soonkyu Hwang[1a], Ikgeun Jeon[1b], Gayoung Han[1c], Hoon Sohn[*1] and Wonjun Yun[2d]

[1]*Department of Civil and Environmental Engineering, Korea Advanced Institute of Science and Technology, Daejeon 34141, South Korea*
[2]*Advanced Research Center, Korea Shipbuilding and Offshore Engineering Co. Ltd., Seoul 03058, South Korea*

(Received July 26, 2019, Revised August 27, 2019, Accepted August 31, 2019)

Abstract. Triplex composite is an epoxy-bonded joint structure, which constitutes the secondary barrier in a liquefied natural gas (LNG) carrier. Defects in the triplex composite weaken its shear strength and may cause leakage of the LNG, thus compromising the structural integrity of the LNG carrier. This paper proposes an autonomous triplex composite inspection (ATCI) system for visualizing and classifying hidden defects in the triplex composite installed inside an LNG carrier. First, heat energy is generated on the surface of the triplex composite using halogen lamps, and the corresponding heat response is measured by an infrared (IR) camera. Next, the region of interest (ROI) is traced and noise components are removed to minimize false indications of defects. After a defect is identified, it is classified as internal void or uncured adhesive and its size and shape are quantified and visualized, respectively. The proposed ATCI system allows the fully automated and contactless detection, classification, and quantification of hidden defects inside the triplex composite. The effectiveness of the proposed ATCI system is validated using the data obtained from actual triplex composite installed in an LNG carrier membrane system.

Keywords: liquefied natural gas (LNG) carrier; active thermography; defect classification and quantification; triplex composites; internal void; uncured adhesive; image processing

1. Introduction

The demand for liquefied natural gas (LNG) has been increasing owing to its low price and low greenhouse gas emissions (Pospíšil *et al*. 2019, IGU 2019). For example, the LNG trade in 2018 reached 316.5 million tons, which represented an increase of 9.8% from 2017 (IGU 2019). Because the volume of LNG expands by more than 600 times when the gas is vaporized, the containment system inside an LNG carrier should maintain the cryogenic temperature (−162℃) and atmospheric pressure (1 atm) during transport. Two types of containment systems are commonly employed in LNG carriers: moss-type and membrane-type (Mokhatab *et al*. 2013). The membrane-type system is generally preferred over the moss-type because its construction is faster and it offers larger space for LNG storage than the moss-type system. However, it requires extra precautions to prevent gas leakage. This study examines a Mark III membrane system designed by Gaztransport & Technigaz SA (GTT) because it occupies 75% of the entire market for LNG containment systems (IGU 2018).

*Corresponding author, Ph.D., Professor
E-mail: hoonsohn@kaist.ac.kr
[a] Graduate student
[b] Graduate student
[c] Graduate student
[d] Ph.D.

The Mark III membrane system is composed of two barriers (primary and secondary barriers) for airtightness, and polyurethane foam is filled between the two barriers for insulation, as shown in Fig. 1. Considering the large volume of the Mark III containment system (266,000 m^3), one of the main technical challenges is to perform timely and reliable inspections of the barriers during construction. The secondary barrier comprises rigid secondary barriers (RSB) and triplex composite connecting these RSBs, as shown in Fig. 2(a) (Kim 2008, Mokhatab *et al*. 2013). The triplex composite connects the two adjacent RSBs by overlaying a flexible secondary barrier (FSB) over the RSB using a bonding layer, as shown in Fig. 2(b). Thus, the triplex composite structure comprises the RSB, bonding layer, and FSB. Here, according to the shape and volume of the Mark III membrane system, there may be areas where the width and shape of the triplex composite is non-uniform. Such triplex composite structures are vulnerable to defects, which often appear inside the bonding layer of the triplex composites and deteriorate the airtightness of the secondary barrier (Costa *et al*. 2001, Zhu *et al.* 2009). Two types of defects commonly appear on triplex composites—internal void and uncured adhesive—as shown in Fig. 2(c). Internal voids can be formed inside the bonding layer between the FSB and RSB during the installation of the bonding and FSB layers (Olivier *et al.* 1995, Agius *et al.* 2013). With regard to adhesive defects, the adhesive is produced by mixing an epoxy/urethane-based material with a hardener. When the ratio of the hardener to the epoxy/urethane-based material is altered from a specified value, the bonding layer is not fully cured, resulting in the uncured adhesive.

http://www.techno-press.com/journals/sss&subpage=7
ISSN: 1738-1584 (Print), 1738-1991 (Online)

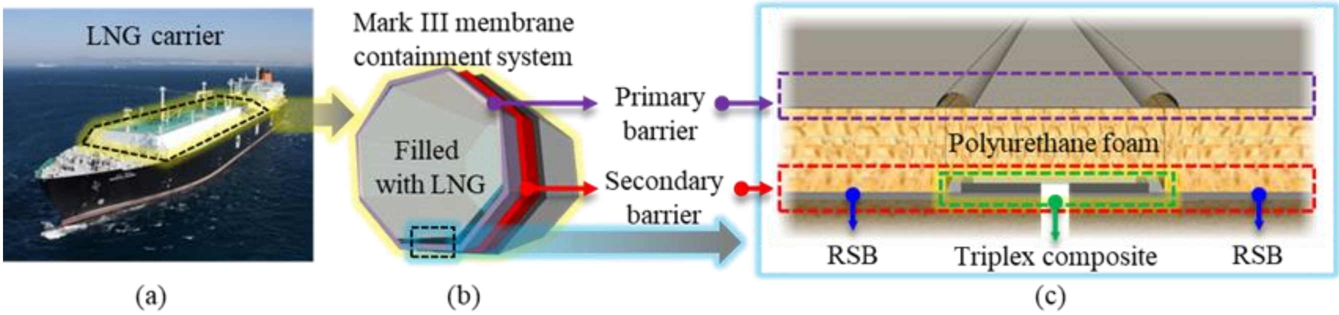

Fig. 1 Overview of Mark III membrane system in LNG carrier: (a) LNG carrier, (b) Mark III membrane-type containment system, and (c) cross-section of Mark III membrane-type containment system comprising primary barrier, second barrier, and polyurethane foam

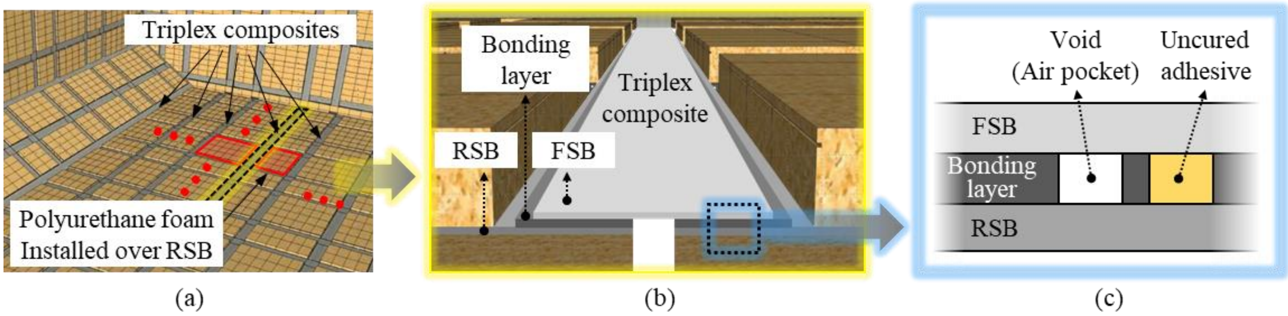

Fig. 2 Overview of secondary barrier: (a) internal view of secondary barrier inside Mark III membrane containment system, (b) triplex composite connecting two adjacent rigid secondary barriers (RSBs) with flexible secondary barrier (FSB) and bonding layer, and (c) void and uncured adhesive inside bonding layer

According to the current GTT guideline, a triplex composite segment should be reinstalled if the diameter of any internal void in it is larger than 12 mm in the transverse direction (perpendicular to the triplex installation direction) or if any uncured adhesive remains (Bonding handbook 2012). However, these defects are invisible from the exposed surfaces because the internal void and the uncured adhesive occur inside the bonding layer between the FSB and RSB. Currently, the triplex composite layers are inspected by manually rubbing a 130-mm-long round metal stick over the surface before the polyurethane foam and the primary barrier are installed over the triplex composites. Considering the installation area of the triplex composite (13 km× 300 mm), this rubbing inspection is very tedious and time-consuming. Furthermore, the inspection result is subjective depending on the inspector, and secondary defects and contamination may occur while rubbing the triplex composite surface.

Non-destructive testing (NDT) techniques have been proposed as alternative inspection options for triplex composites. Li *et al.* (2011) and Maguire (2011) detected defects in triplex composites by measuring the acoustic (elastic) wave radiation in the triplex composite when the material undergoes irreversible changes in its internal structure. However, baseline data are required for signal processing, and false alarms can be triggered by external loading. Moreover, the acoustic emission technique requires contact-type acoustic transducers for measurement and it can detect only the defects that appear after the installation of the transducers. Alternatively, an air-coupled ultrasonic technique performs contactless inspection of triplex composite by generating and measuring ultrasonic waves (Sunarsa *et al.* 2017). Baseline-free and autonomous defect detection can be carried out and the defect size can be estimated through c-scan inspection. However, the inspection requires two-dimensional scanning and is time consuming because multiple measurements are necessary to reduce noise.

In this study, an autonomous triplex composite inspection (ATCI) system is developed based on active thermography for real-time inspection of voids and uncured adhesive in triplex composites. The present study employs the active thermography technique previously developed by the authors (Song *et al.* 2015, Lee *et al.* 2017). A hardware system for the inspection of triplex composite is developed considering the variation in width of the triplex composite layer and the floor angle variation at corner sections. Furthermore, defect visualization and classification algorithms are proposed so that voids and uncured adhesive can be automatically visualized and classified without the baseline data corresponding to the pristine condition of the target triplex composite. The proposed ATCI system offers the following advantages over the previous thermography technique: (1) autonomous detection and classification of internal void and uncured adhesive inside the triplex composites; (2) visualization and quantification of each defect; (3) capable of inspecting triplex composites of varying widths and in corner sections; and (4) validation using real triplex composites installed on the Mark III membrane systems.

This paper is organized as follows. The hardware configuration of the ATCI system along with its working principle is described in Section 2. Autonomous hidden defect visualization and classification algorithms are proposed in Section 3. The effectiveness of the ATCI system is validated using multiple triplex composites in Section 4. Finally, the paper is summarized and concluding remarks are presented in Section 5.

2. Development of autonomous triplex composite inspection (ATCI) hardware

Fig. 3 shows the schematic overview of the proposed ATCI hardware, which consists of three units: (1) an inspection unit comprising an IR camera and two halogen lamps; (2) an alignment unit consisting of a pneumatic device and guidance frame for adjusting the position of the inspection unit; (3) a control unit consisting of an industrial computer and a programmable logic controller (PLC) for controlling the inspection and alignment units and data processing. The inspection unit is mounted on the guidance frame, and the control unit is connected to the inspection unit using industrial cables.

The standard operating sequence of the ATCI system is as follows. First, the ATCI hardware is placed above the target triplex composite and supported by the polyurethane foams surrounding the triplex composite. The width of the guidance frame is adjusted by the pneumatic device so that the frame fits between two polyurethane foams, as shown in Fig. 3. Accordingly, the position of the inspection unit mounted on the guidance frame is adjusted so that the IR camera inside the inspection unit is centered with respect to the width of the triplex composite. The industrial computer transmits the control signal to the PLC, which turns on the halogen lamps to radiate heat energy on the triplex composite. Simultaneously, the IR camera triggered by the halogen lamps records the surface temperature of the triplex composite as IR images. Then, the measured IR images are transmitted to the control unit and analyzed for defect detection, classification, and visualization. Finally, the inspection results are displayed on the monitor mounted on the control unit. After the inspection sequence is complete, the pressure on the pneumatic device is released, and the ATCI system moves onto the next inspection segment of the triplex composites. The details of the IR image analysis algorithms are described in Section3.

3. Development of autonomous hidden defect visualization and classification algorithm

When the ATCI system turns the halogen lamps on and off, the surface temperature of the triplex composite fluctuates accordingly. If a defect exists inside the triplex composite, the heating and cooling characteristics of the target surface deviate from the normal characteristics. In this section, a statistical pattern recognition algorithm is presentedto autonomously detect, visualize, and classify hidden defects from the IR images of the triplex composite. Fig. 4 describes the four steps of the proposed algorithm.

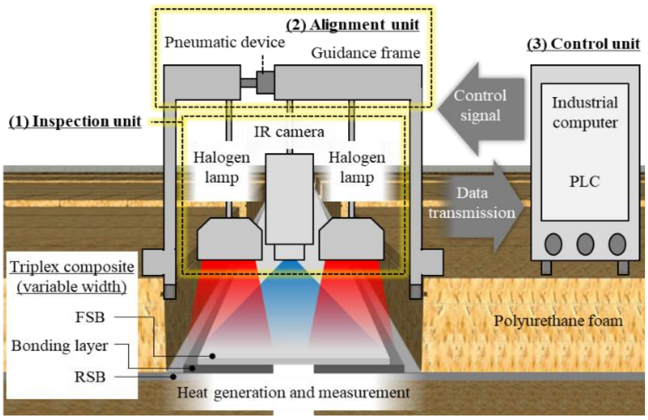

Fig. 3 Overview of the autonomous triplex composite inspection (ATCI) hardware: (1) inspection unit consisting of two halogen lamps and an infrared (IR) camera, (2) alignment unit consisting of a pneumatic device and a guidance frame, and (3) control unit consisting of an industrial computer and a programmable logic controller (PLC)

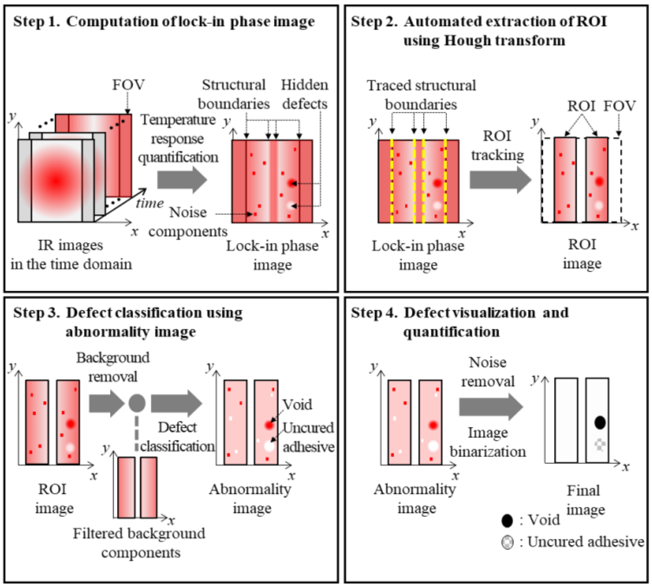

Fig. 4 Overview of autonomous hidden defect visualization and classification algorithm

Step 1. Computation of lock-in phase image

After the ATCI hardware has collected the temperature responses from the field of view (FOV) of the IR camera (Fig. 5(a)) as multiple IR images (I_t) in the time domain, a lock-in phase image (P) is computed from the IR images, as follows (Busse *et al.* 1992)

$$P(x,y) = \tan^{-1}\left(\frac{I_0(x,y)-I_\tau(x,y)}{I_\tau(x,y)-I_T(x,y)}\right), \tag{1}$$

where the subscripts 0, τ, and T denote the starting and ending time of the heating, and the duration of IR image collection, respectively; these are depicted in Fig. 5(b). The lock-in phase image described in Eq. (1) exhibits temperature responses synchronized with the halogen lamp excitation. Here, the external temperature responses, which are not synchronized with halogen lamp, do not appear in the lock-in phase image. The defects and structural boundaries of the triplex composite are visualized, as shown in Fig. 5(c). The structural boundaries represent the discontinuities where the thickness and composition of the triplex composite suddenly changes, as illustrated in Fig. 5(a). It has been reported that the lock-in phase image is sensitive to subsurface defects, whereas the lock-in amplitude image is more effective in detecting surface defects (Meola andCarlomagno2004, Choi *et al*. 2008).

Step 2. Automated extraction of ROI (Region of Interest) using Hough transform

As mentioned previously, the width of the triplex composite varies inside the Mark III membrane containment system. Therefore, the ROI should be automatically extracted from the FOV of the IR image for each inspection. The ROI is defined as the area where the FSB is attached to the RSB using the bonding layer, as shown in Fig. 6. The ROI is confined by four external and internal structural boundaries created by the sudden changes in the thickness and composition ofthe triplex composite. Furthermore, the structural boundaries also appear in the lock-in phase image, as shown in Fig. 5(c). In this study, the Hough transform is applied to the lock-in phase image for the extraction of these structural boundaries (Duda and Hart 1971, Yang *et al.* 2016).

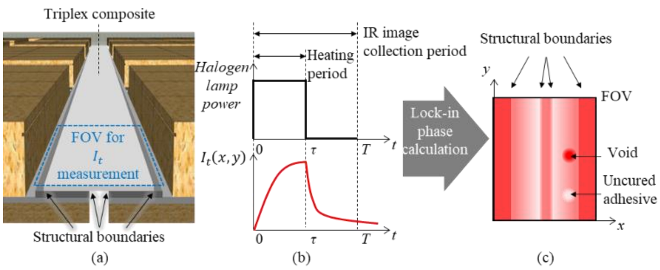

Fig. 5 Computation of a lock-in phase image from IR image sequences (I_t) obtained in the time domain: (a) triplex composite and field of view (FOV) of the IR camera, (b) temperature response corresponding to the halogen lamp at a specific spatial point (x, y) of I_t, and (c) lock-in phase image (P)

First, the edge image is obtained by applying Canny edge filtering to the lock-in phase image, and various edge components, including the structural boundaries, appear in the edge image, as shown in Fig. 7(a) (Nadernejad *et al.* 2008). Then, the edge components expressed in the Cartesian coordinates are transformed into the Hough coordinates, as follows

$$r = x \cdot cos\,\theta + y \cdot sin\,\theta \tag{2}$$

where x and y represent the coordinates of a single point in the Cartesian coordinate system, and r and θ represent the normal distance and orthogonal angle of an arbitrary straight line crossing the single point in the Hough coordinate system. According to Eq. (2), the collection of all straight lines crossing a single point A in the Cartesian coordinate system (Fig. 8(a)) is represented as a single curved line in the Hough coordinate system (Fig. 8(c)) (Mukhopadhyay and Chaudhuri 2015, Yang *et al*. 2016). Similarly, the collections of all straight lines crossing points B and C (Fig. 8 (b)) are also represented as curved lines b and c, respectively, in the Hough coordinate system (Fig. 8 (d)).Note that the straight line through points B and C in the Cartesian coordinate system passes through the crossing point of the curved lines b and c in the Hough coordinate system.

Thus, after applying the Hough transform to the edge image, the line components in the edge image can be identified by finding the crossing points of multiple curved lines in the Hough image, as shown in Fig. 7(b). Furthermore, the structural boundaries, which are represented by a continuous line, can be extracted by inverse Hough transform of the dominant crossing points in the Hough coordinate system, as shown in Fig. 7(c).

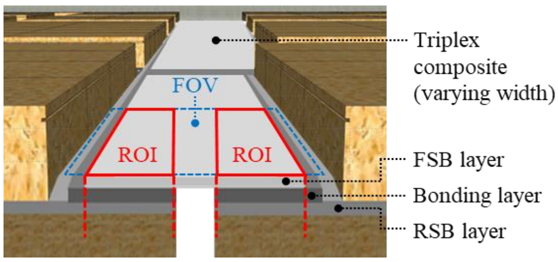

Fig. 6 Illustration of the region of interest (ROI) on the triplex composite

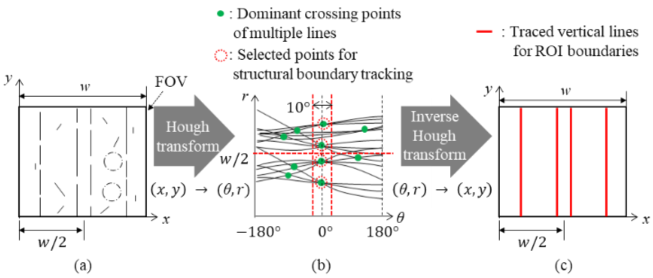

Fig. 7 Extraction of structural boundaries using Hough transform: (a) edge image, (b) Hough image, and (c) structural boundaries for ROI extraction

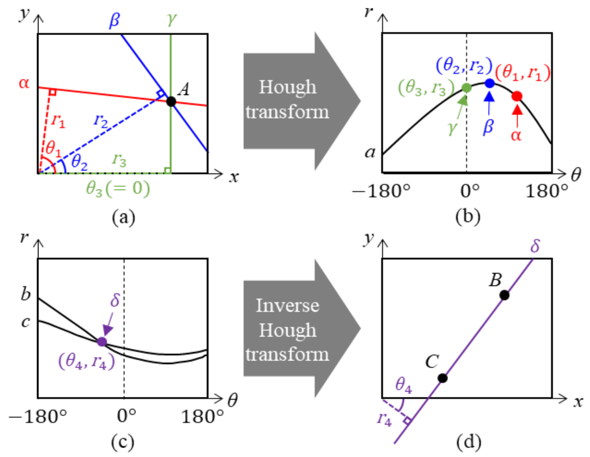

Fig. 8 Principle of Hough transform: (a) multiple straight line features (α, β, and γ) passing a single point (A) in the Cartesian coordinate system, (b) multiple points (α, β, and γ) on a single curved line (a) in the Hough coordinate system, (c) single point (δ) at the crossing point of two curved lines (b and c) in the Hough coordinate system, and (d) single straight line feature (δ) passing two points (B and C) in the Cartesian coordinatesystem

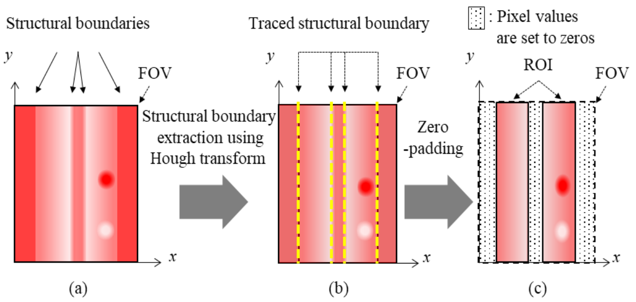

Fig. 9 Extraction of ROI from FOV: (a) FOV of lock-in phase image, (b) traced vertical lines using the Hough transform, and (c) ROI image

Because the local orientation of the structural boundaries can slightly deviate from the straight line in practice, $\pm 5°$ of margin is added to θ for the extraction of the structural boundaries. Finally, the ROI is extracted from the FOV, and the ROI image is obtained by setting the pixel values outside the ROI to zeros, as shown in Fig. 9.

Step 3. Defect classification using abnormality image

The defects in the triplex composites produce abnormal temperature responses on the ROI image, but additional abnormal patterns may also appear owing to heat energy accumulation around the vertical and horizontal structural boundaries of the ROI image due to sudden changes in thermal conductivity, as shown in Fig. 10(a). The abnormality caused by the structural boundaries is often spread out over a large area whereas the abnormality produced by the defect is localized. Here, a spatial 2-dimensional (2D) fast Fourier transform (FFT) filtering is used to remove the abnormality associated with the structural boundaries based on its unique spatial characteristics. First, the ROI image (R) is transformed into the frequency domain image (F) using the spatial 2D FFT, as follows (Fig. 10 (b))

$$F(u, v) = \sum_{x=0}^{M-1} \sum_{y=0}^{N-1} R(x, y) e^{-i2\pi\left(\frac{ux}{M}+\frac{vy}{N}\right)} \tag{3}$$

where M and N are the number of pixels along the x and y axes, and u and v are the spatial frequencies of pixels values along the x and y axes, respectively. Note that the 2D FFT filtering is applied individually to each segment of the ROI image. The abnormal vertical pattern created by the structural boundaries appears as a horizontal line in the frequency image, and vice versa. A notch filter (H) is applied to the vertical and horizontal directions of the frequency domain image to remove the patterns created by the structural boundaries. Then, the notch-filtered image ($F_{filtered}$) shown in Fig. 10(c) is applied.

$$F_{filtered}(u, v) = H(u, v) F(u, v) \tag{4}$$

$$H(u, v) = \begin{cases} 0 & -1 \le u \le 1, or -1 \le v \le 1 \\ 1 & otherwise \end{cases} \tag{5}$$

Next, the abnormality image (A) is obtained using a 2D inverse FFT, and the abnormality associated only with the hidden defects remains in the abnormality image, as follows (Fig. 10(d))

$$A(x, y) = 1/MN \sum_{u=0}^{M-1} \sum_{v=0}^{N-1} F_{filtered}(u, v) e^{j2\pi\left(\frac{ux}{M}+\frac{vy}{N}\right)}. \tag{6}$$

The aforementioned procedures are performed for each segment of the ROI. Note that $F(0,0)$ represents the mean value of the ROI image. Thus, after applying notch filtering to the frequency domain image, the pixel values associated with the intact region of the abnormality image approach zero.

Note that the characteristics of the temperature response vary depending on the presence and types of defects inthe triplex composite. For example, the surface temperature of the triplex composite increases more rapidly around the internal void than in the intact area, as indicated by the red dotted line in Fig. 11.

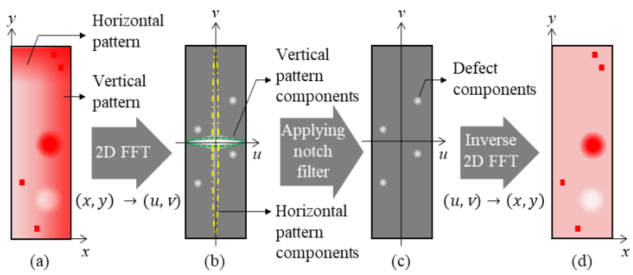

Fig. 10 Image processing for defect classification: (a) ROI image, (b) frequency domain image, (c) notch-filtered image, and (d) abnormality image

The thermal conductivity of the air inside the internal void (0.026 $W \cdot m^{-1} \cdot K^{-1}$) is 50 times lower than that of the normal bonding layer. Thus, the heat energy on the triplex composite surface passes through the void more slowly because of which the local area shows higher temperature than the surrounding intact area. On the contrary, the uncured adhesive experiences a lower rise in temperature than the intact area, but the temperature variation caused by the uncured adhesive is more subtle than that caused by the internal void, as indicated by the blue dashed line in Fig. 11 (Cengel *et al.* 2012). The lock-in phase value represents the relative speed of the temperature variation, as shown in Eq. (1).Therefore, the internal void can be located by identifying the area where the abnormality value is larger than zero, as shown in Fig. 12(b). An abnormality value larger than zero indicates that the temperature of the corresponding area increases more rapidly than that of the surrounding intact area. Similarly, the uncured adhesive can be detected by finding the area with a negative abnormality value, as shown in Fig. 12(c).

Step 4. Defect visualization and quantification

Statistical denoising is applied to the abnormality image to remove sporadic salt and pepper noise components, as shown in Fig. 13.The non-zero-pixel values in the abnormality image are divided into two groups: Group I with positive pixel values and Group II with negative pixel values. Here, the zero-pixel values in the abnormality image are defined as intact region. For void detection, the Weibull distribution is fitted to the absolute values of Group I data. For uncured adhesive, a Gaussian distribution is fitted to the absolute values of Group II data. Then, a threshold value corresponding to a one-sided 99% confidence interval of the cumulative density function (either Weibull or Gaussian)in the upper tail is calculated. Using the threshold value, a binary image (B) is computed from the abnormality image (A), as follows

$$B(x,y) = \begin{cases} 1 & if \;\; A(x,y) \geq Threshold \;\; (from \;\; Group \;\; I) \\ -1 & if \;\; A(x,y) \leq Threshold \;\; (from \;\; Group \;\; II). \\ 0 & \qquad\qquad otherwise \end{cases} \tag{7}$$

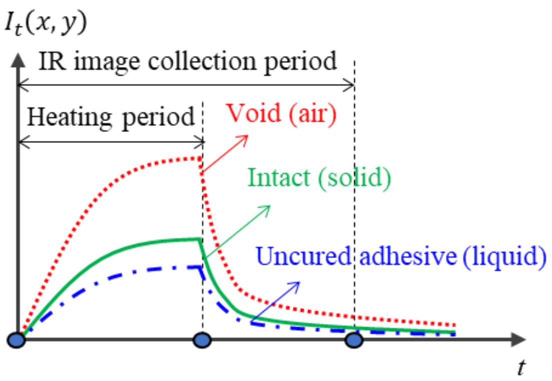

Fig. 11 Variations in temperature response characteristics depending on the presence of defects

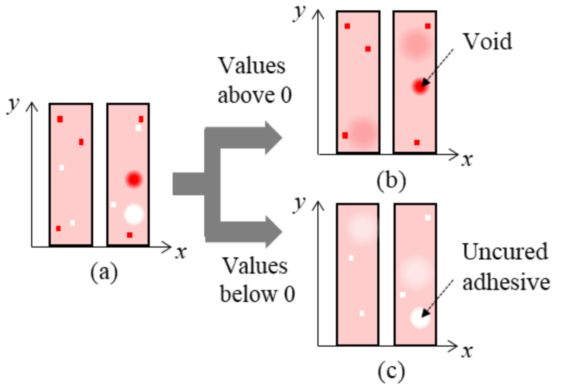

Fig. 12 Defect classification using the abnormality image: (a) abnormality image, (b) internal void, and (c) uncured adhesive

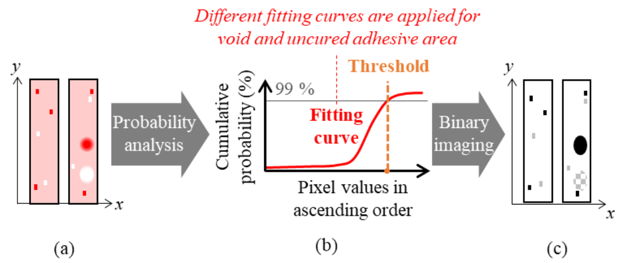

Fig. 13 Statistical denoising for improved defect visualization: (a) abnormality image, (b) threshold establishment for noise cancellation, and (c) binary image

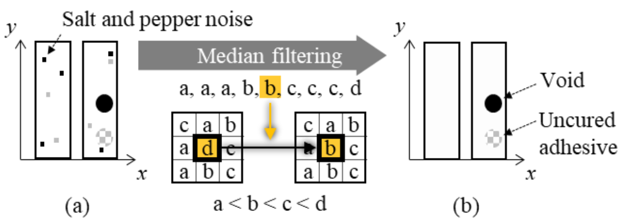

Fig. 14 Construction of the final image after median filtering: (a) binary image and (b) final image

Finally, a median filter with a mask size of 3×3 is applied to the binary image, and the final image is constructed as shown in Fig. 14. The defect size is quantified by counting the number of pixels within each defect.

4. Experimental validation

4.1. Description of target triplex composites

To validate the performance of the proposed ATCI system, experimental tests were performed with real triplex composites used inan LNG membrane system manufactured by Hyundai Heavy Industries Co., Ltd. The triplex composites composed of FSB, bonding layer, and RSB were laid over the polyurethane foam, as shown in Figs. 15(a) and 15(b). The width of the triplex composites was varied from 250 mm to 450 mm along the longitudinal direction and the width of the ROI changed accordingly. Totally, 16 triplex composite specimens were fabricated for the validation tests. Eight of the specimens were intact, one specimen had both internal void and uncured adhesive, and the remaining seven specimens had either internal void or uncured adhesive defect. Figs. 15(c)-15(e) show the images of the intact bonding layer, the internal void, and the uncured adhesive, respectively. These images were acquired after peeling off the FSB layer after the inspection.

4.2. Experimental setup

Fig. 16 shows the proposed ATCI hardware system placed over the polyurethane foam and the target inspection area of the triplex composites. The dimensions and weight of the ATCI system were $500 \times 350 \times 400$ mm^3 (width $\times$ length $\times$ height) and 22 kg, respectively. An IR camera (A65SC, FLIR Systems, Inc.) with spatial resolution of 705 μm for 300×450 mm^2 FOV, 0.03 K temperature resolution, and spectral range of 7.5 ~ 13 μm was installed 250 mm above the triplex composites. The width of the ROI changed according to the change in the width of the triplex composite. However, the height of the ROI was fixed at300 cm. Custom-made halogen lamps with output power of 3.9 kW were placed 235 mm above the triplex composites.

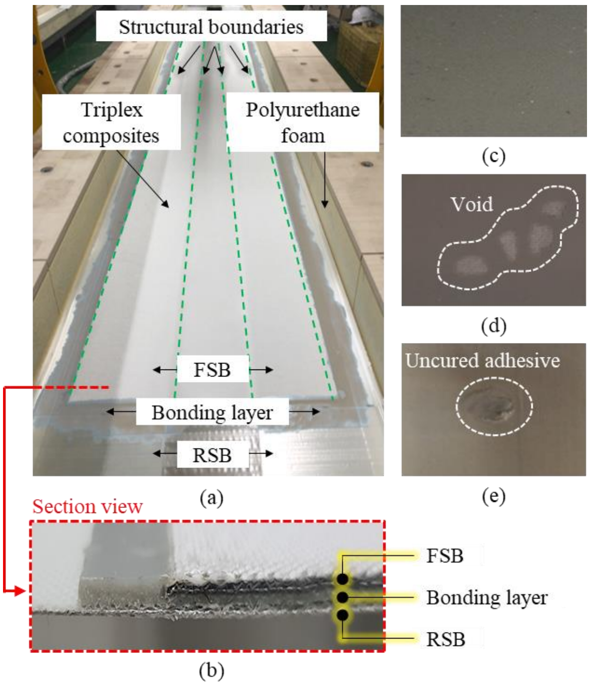

Fig. 15 Triplex composites used for experimental validation: (a) triplex composites installed on the polyurethane foam, (b) cross-section view of triplex composites, (c) intact area, (d) internal void, and (e) uncured adhesive inside the bonding layer

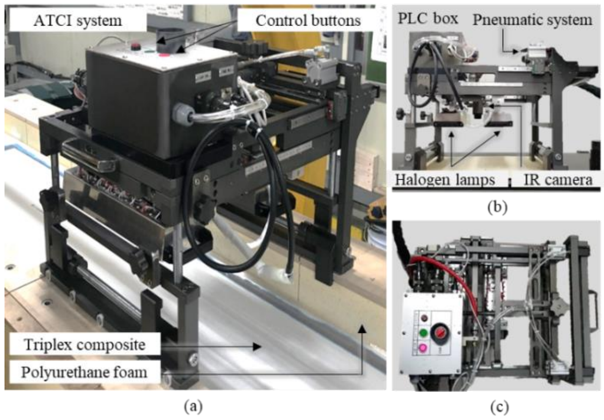

Fig. 16 Experimental setup of the proposed ATCI hardware system: (a) ATCI system placed on the triplex composite, (b) side view of ATCI system and (c) top view of ATCI system

The pneumatic device produced a pressure of 100 psi to adjust the length of the frame arm and the position of the halogen lamps. The industrial computer (ECS9200, Vecow Co., Ltd.) was equipped with a 3.60-GHz quad-core processor and 8-GB memory, and the PLC (XBC-DR20SU, LS Industrial Systems Co., Ltd.) transmitted control signals with a time delay of less than 92 ns.

When the control button on the ATCI system was pressed, the halogen lamps were turned on for 6 s to generate heat energy on the target surface. Simultaneously, the IR camera recorded the temperature responses of the target surface for 10 s at a sampling frequency of 1 Hz. After the IR images were captured, defect visualization and classification were performed automatically inside the industrial computer.

4.3 Experimental results

Fig. 17 shows the representative IR images recorded at 0, 6, and 12 s after the IR camera started recording. Here, the halogen lamps were turned on and off at 0 and 6 s, respectively. Next, the lock-in phase image was computed from the raw IR images, as shown in Fig. 18(a). Subsequently, the Hough image was constructed by applying the Hough transform to the lock-in phase image. The angle and position (x-axis) of the vertical lines within the ROI were traced by identifying the crossing points of the multiple lines in the Hough image, as shown in Fig. 18(b). Then, the ROI image was obtained by setting the pixel values located outside the structural boundaries of the lock-in phase image to zeros, as shown in Fig. 18(c).

To cancel out the undesired abnormal temperature responses caused by the structural boundaries, the ROI image was transformed to the frequency domain using the spatial 2D FFT, as shown in Fig. 19(a), and the undesired abnormalities were removed using notch filtering. Then, the abnormality image was computed through 2D inverse FFT, as shown in Fig. 19(b). A comparison of Figs. 18(c) and 19(b) shows that the undesired abnormal temperature responses caused by the structural boundaries are successfully removed but the abnormalities induced by the internal void and uncured adhesive are retained. Then, the defects were classified as void or uncured adhesive based on the abnormality pixel values (void if the pixel value is larger than zero, and uncured adhesive if the pixel value is smaller than zero). The abnormality images for internal void and uncured adhesive are shown in Figs. 19(c) and 19(d) after normalizing the pixel values between 0 and 1. Lastly, the final image was constructed after applying the median filters to the two abnormality images and merging them into a single image, as shown in Fig. 20. The sizes of the two internal voids were estimated to be 31.9 mm and 23.5 mm in the transverse (x) direction. Their actual sizes were 30 mm and 25 mm. The size of the 35.0-mm uncured adhesive was estimated to be 35.5 mm. Here, the actual size of each defect was estimated through the X-ray image, as shown in Fig. 21.

Fig. 22 shows the defect visualization results for the eight defective test triplex composite specimens with varying width and floor angle variation at corner section. Note that no indication of defects was found in the other eight intact specimens, and their results are not shown here owing to space limitation. All internal voids and uncured adhesives larger than 7 mm in the transverse direction were successfully identified without any false positives. The inspection results were compared with the actual bonding conditions by peeling-off the FSB layer after each inspection. The overall defect size estimation error was less than 2 mm. This inspection performance meets the GTT guideline for quality control of the triplex composite, which states that (1) all internal voids larger than 12 mm in the transverse direction should be detected and (2) any uncured adhesive should be detected, as explained in Section1.

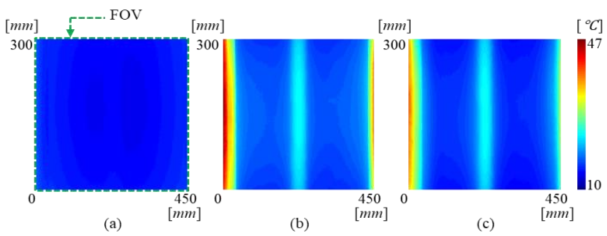

Fig.17 IR images acquired at (a) 0 s, (b) 6 s, and (c) 12 s

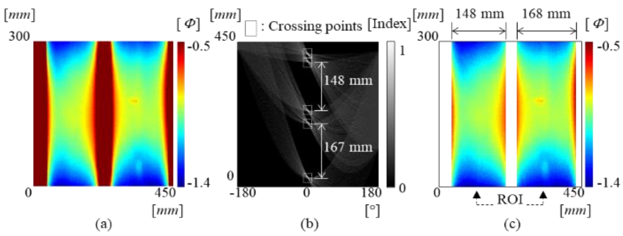

Fig. 18 Extraction of structural boundaries using Hough transforms: (a) lock-in phase image, (b) Hough image, and (c) ROI image

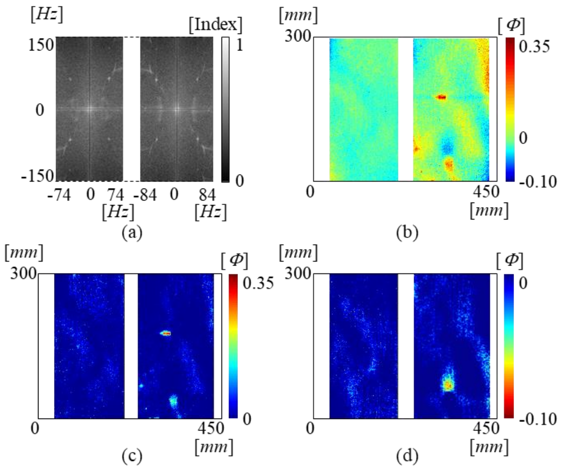

Fig. 19 Defect classification using abnormality image: (a) frequency images, (b) abnormality images, (c) abnormality images for internal void, and (d) abnormality images for uncured adhesive

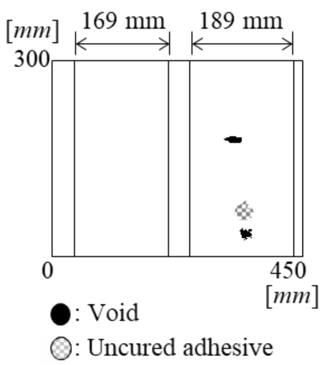

Fig. 20 Final image with defect visualization and classification

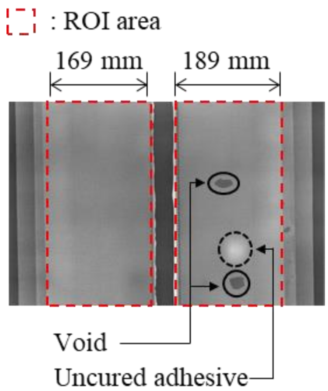

Fig. 21 X-ray image of the target triplex composites

Moreover, the ROI was successfully identified for all specimens with less than 2-mm errors. The total computation time for defect visualization and classification of each inspection area was less than 1s using MATLAB R2018a software program on a 3.60-GHz quad-core

processor. Note that, additional blind tests of the proposed ACTI system were performed at the real construction site of the LNG carrier membrane system.
However, the blind test results were not included in this paper due to the confidential issues.

5. Conclusions

In this study, an autonomous triplex composite inspection (ATCI) system was developed to automatically visualize and classify the internal void and uncured adhesive defects in triplex composites of membrane systems used in LNG carriers. First, the ATCI system heats the triplex composite surface using halogen lamps and measures the corresponding temperature responses of the triplex composite surface using an IR camera. Then, the measured temperature responses are analyzed based on multiple image processing and statistical pattern recognition algorithms.

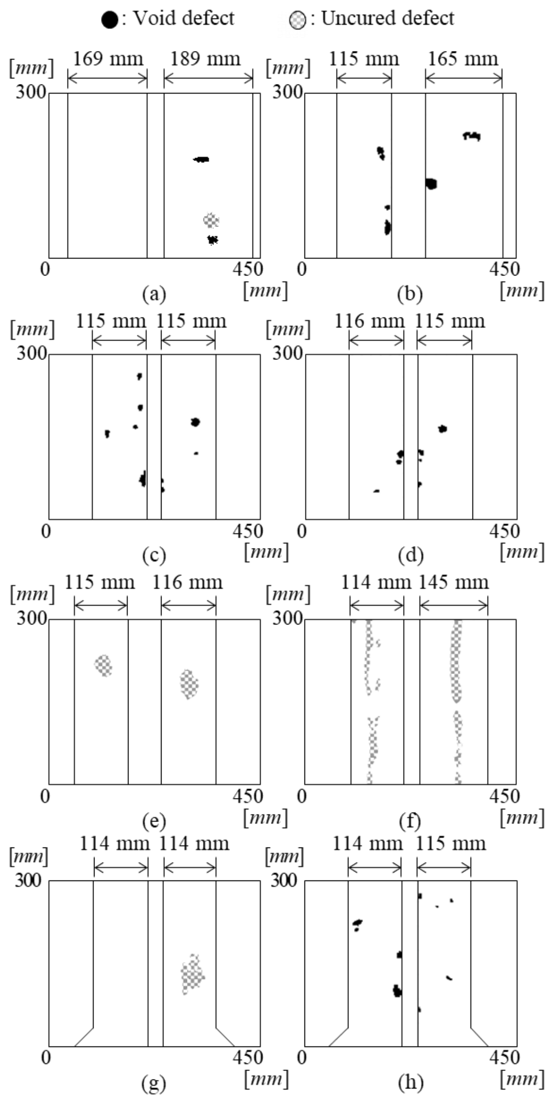

Fig. 22 Detection of void and uncured adhesive in triplex composite specimens with varying width and floor angle variation at corner section

The uniqueness of the proposed ATCI system is that it can non-destructively and non-invasively inspect triplex composites during LNG carrier construction in real-time. Particularly, the proposed algorithm installed in the ATCI system enables automated visualization, classification, and quantification of defects commonly found in triplex composites. The performance of the ATCI system was examined using 16 actual triplex composite specimens installed on the Mark III membrane structure of an LNG carrier. All internal voids and uncured adhesives were successfully detected without any false positives. The defect size was quantified with an accuracy of approximately$\pm$2mm. The ATCI system can inspect triplex composites with a speed of 1.8 m^2/min, which is faster than the current manual rubbing inspection speed. The proposed ATCI system is expected to improve the productivity and quality of triplex composite installation by enabling faster and more reliable inspection of the triplex composite than possible with the currently used manual metal stick rubbing inspection.

Acknowledgments

This research was supported by a grant(19CTAP-C152129-01) from Technology Advancement Research Program(TARP) funded by Ministry of Land, Infrastructure and Transport of Korean government, and HHI-KAIST Cooperative Research program of Hyundai Heavy Industries Inc.

References

Agius, S., Magniez, K. and Fox, B. (2013), "Cure behaviour and void development within rapidly cured out-of-autoclave composites", *Comps. Part B-Eng.*, **47**, 230-237. DOI: 10.1016/j.compositesb.2012.11.020.

BuSSe, G., Wu, D. and Karpen, W. (1992), "Thermal wave imaging with phase sensitive modulated thermography", *J. Appl. Phys.*, **71**(8), 3962-3965. DOI: 10.1063/1.351366.

Cengel, Y.A., Cimbala, J.M., Turner, R.H. and Kanoglu, M. (2012), Fundamentals of thermal-fluid sciences (Vol. 3): McGraw-Hill Higher Education Boston.

Choi, M., Kang, K., Park, J., Kim, W. and Kim, K. (2008), "Quantitative determination of a subsurface defect of reference specimen by lock-in infrared thermography", *Ndt &E Int.*, **41**(2), 119-124. DOI: 10.1016/j.ndteint.2007.08.006.

Costa, M.L., De Almeida, S.F.M. and Rezende, M.C. (2001), "The influence of porosity on the interlaminar shear strength of carbon/epoxy and carbon/bismaleimide fabric laminates", *Comps. Sci. Technol.*, **61**(14), 2101-2108. DOI: 10.1016/S0266-3538(01)00157-9.

Duda, R.O. and Hart, P.E. (1971), "Use of the Hough transformation to detect lines and curves in pictures", *Commun. Acm.*, **15**(1), 11-15. DOI: 10.1145/361237.361242.

IGU. (2018), IGU 2018 World LNG Report. In: International gas union.

IGU. (2019), IGU 2019 World LNG Report. In: International gas union.

Kim, B.G. (2008), "Leakage characteristics of the glass fabric composite barriers of LNG ships", *Compos. Struct.*, **86**(1-3), 27-36. DOI: 10.1016/j.compstruct.2008.03.021.

Lee, S., Lim, H.J., Sohn, H., Yun, W. and Song, E. (2017), "Autonomous mobile lock-in thermography system for detecting and quantifying voids in liquefied natural gas cargo tank second barrier", *Struct. Health Monit.*, **16**(3), 276-290. DOI: 10.1177/1475921716651810.

Li, H., Li, J., Yun, X., Liu, X. and Fok, A.S.L. (2011),"Non-destructive examination of interfacial debonding using acoustic emission", *Dent. Mater.*, **27**(10), 964-971. DOI: 10.1016/j.dental.2011.06.002.

Maguire, J.R. (2011), "Acoustic emission monitoring of composite containment systems", *J. Phys.*, **305**(1). DOI: 10.1088/1742-6596/305/1/012044.

Meola, C. and Carlomagno, G.M. (2004), "Recent advances in the use of infrared thermography", *Meas. Sci. Technol.*, **15**(9), R27.

Mokhatab, S., Mak, J.Y., Valappil, J.V. and Wood, D.A. (2013). Handbook of liquefied natural gas: Gulf Professional Publishing.

Mukhopadhyay, P. and Chaudhuri, B.B. (2015), "A survey of Hough Transform", *Pattern Recogn.*, **48**(3), 993-1010. DOI: 10.1016/j.patcog.2014.08.027.

Nadernejad, E., Sharifzadeh, S. and Hassanpour, H. (2008), "Edge detection techniques: Evaluations and comparisons", *Appl. Math. Sci.*, **2**(31), 1507-1520.

Olivier, P., Cottu, J. and Ferret, B. (1995), "Effects of cure cycle pressure and voids on some mechanical properties of carbon/epoxy laminates", *Compos.*, **26**(7), 509-515. DOI: 10.1016/0010-4361(95)96808-J.

Pospíšil, J., Charvat, P., Arsenyeva, O., Klimeš, L., Špiláček, M. and Klemeš, J.J. (2019), "Energy demand of liquefaction and regasification of natural gas and the potential of LNG for operative thermal energy storage", *Renew. Sust. Energ. Rev.*, **99**, 1-15. DOI: 10.1016/j.rser.2018.09.027.

Song, H., Lim, H. J., Lee, S., Sohn, H., Yun, W. and Song, E. (2015), "Automated detection and quantification of hidden voids in triplex bonding layers using active lock-in thermography", *Ndt & E Int.*, **74**, 94-105. DOI: doi.org/10.1016/j.ndteint.2015.05.004.

Technigaz, G. (2012), Bonding handbook: Saint-Re´my-le`s-Chevreuse: Gaztransport&Technigaz.

Yang, J., Choi, J., Hwang, S., An, Y.K. and Sohn, H. (2016), "A reference-free micro defect visualization using pulse laser scanning thermography and image processing", *Meas. Sci. Technol.*, **27**(8), 085601. DOI: 10.1088/0957-0233/27/8/085601.

YonathanSunarsa, T., Aryan, P., Jeon, I., Park, B., Liu, P. and Sohn, H. (2017), "A reference-free and non-contact method for detecting and imaging damage in adhesive-bonded structures using air-coupled ultrasonic transducers", *Materials*, **10**(12), 1402. DOI: 0.3390/ma10121402.

Zhu, H.Y., Li, D.H., Zhang, D.X., Wu, B.C. and Chen, Y.Y. (2009), "Influence of voids on interlaminar shear strength of carbon/epoxy fabric laminates", *Trans. Nonferrous Met. Soc. China*, **19**, s470-s475. DOI: 10.1016/S1003-6326(10)60091-X.